Breakup prediction of oscillating droplets under turbulent flow

Camille Deberne, Victor Chéron, Alexandre Poux, Jorge César Brändle de Motta

To cite this version:

Camille Deberne, Victor Chéron, Alexandre Poux, Jorge César Brändle de Motta. Breakup prediction of oscillating droplets under turbulent flow. International Journal of Multiphase Flow, 2024, 173, pp.104731. 10.1016/j.ijmultiphaseflow.2024.104731 . hal-04408853

HAL Id: hal-04408853
https://hal.science/hal-04408853v1

Submitted on 22 Jan 2024

International Journal of Multiphase Flow 173 (2024) 104731

Contents lists available at ScienceDirect

International Journal of Multiphase Flow

journal homepage: www.elsevier.com/locate/ijmulflow

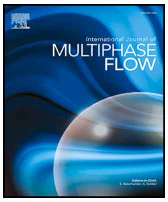

Breakup prediction of oscillating droplets under turbulent flow

Camille Deberne [a,1], Victor Chéron [a,b,1], Alexandre Poux [a], Jorge César Brändle de Motta [a,*]

[a] Univ Rouen Normandie, INSA Rouen Normandie, CNRS, CORIA UMR 6614, F-76000 Rouen, France
[b] Lehrstuhl für Mechanische Verfahrenstechnik, Otto-von-Guericke-Universität Magdeburg, Universitätsplatz 2, 39106 Magdeburg, Germany

ARTICLE INFO

Keywords:
Drops and bubbles
Turbulence
Breakup
Direct numerical simulation (DNS)
Shape parameters

ABSTRACT

Droplet and bubble breakup phenomena under turbulent flow have been widely studied for over 70 years through theoretical, experimental and numerical approaches. Despite significant progress, the dynamics of breakup remains an active research topic. The present study considers a database of breakup events under turbulent conditions. The database contains neutrally buoyant droplets obtained for a single moderate turbulent Reynolds number and a Weber number near the critical Weber number of the droplets, allowing for long time evolution prior to droplet breakage. Each droplet in the database follows a consistent behavior: the droplet undergoes (1) an initial shape deformation, then (2) an extended oscillatory regime, until (3) a critical large deformation starts, leading to (4) a capillary-driven breakup. While the first two stages have been investigated in our previous work using spherical harmonics decomposition, this study focuses on the last two stages, describing them qualitatively and quantitatively by means of seven different shape parameters. These shape parameters are based on different information of the specific droplet such as its surface, its volume or its averaged mean curvature, and provide a multidimensional analysis of the droplet breakup. They are used to measure the time spent in the final two stages prior to breakup, as well as the transition between these stages. Additionally, we establish breakup thresholds for each shape parameter to predict neutrally buoyant droplet breakup under turbulent flow conditions.

1. Introduction

Breakup of bubbles and droplets constitutes a complex phenomenon involving several mechanisms such as interface shearing or interfacial instabilities (Liao and Lucas, 2009; Solsvik et al., 2013). The process of breakup under turbulent conditions leads to different regimes influenced by the properties of both the dispersed and carrier fluids, and by the intensity of turbulence in the flow (Lefebvre and McDonell, 2017; Deike, 2022; Ni, 2024). While addressing the complexity of this process, two common methods are employed: the derivation of population balance models, which account for the number of droplets (Wieringa et al., 1996), and the treatment of individual breakup events using a Lagrangian approach (O'Rourke and Amsden, 1987). Both methods are based on understanding the mechanisms underlying droplet fragmentation in turbulent flows. For studying turbulence-induced breakup, two main experiments are often considered (see the introduction of Håkansson (2020) for a detailed discussion). The first involves the analysis of the complete system (*e.g.* jet in a combustion chamber, stirred tanks) and the derivation of the model by inversion of the problem: such a model predicts the size probability density function. The second approach focuses on studying isolated breakup events of bubbles or droplets under turbulent conditions and derive directly the model predicting breakup. The results obtained from both approaches raise many questions that are still under consideration. For instance, what is the timescale for turbulence to break a given droplet or bubble? Why do some droplets break under similar conditions while others do not? Which parameter best predicts droplet breakup under turbulent flow?

Numerous authors have already addressed these questions using theoretical, experimental, or numerical approaches, and considering liquid–liquid, liquid–gas, and gas–liquid mixtures (Ni, 2024). The earliest theoretical studies on this subject date back to the 1950s and were conducted by Kolmogorov (1949) and Hinze (1955). They investigated the balance between turbulence intensity and surface tension, introducing the well-known 'Hinze diameter' criterion and its subsequent extensions. These criteria are valuable to predict the order of magnitude of final droplet/bubble sizes in turbulent environments, but they fail to provide a detailed temporal sequence prior to breakup. For droplets and bubbles close to or below the critical length, known as the sub-Hinze scale, the breakup process is often described as a statistical phenomenon (Liao and Lucas, 2009; Solsvik et al., 2013), with the droplets oscillating due to turbulent flows for extended periods before

---

[*] Corresponding author.
E-mail address: jorge.brandle@coria.fr (J.C. Brändle de Motta).
[1] These authors contributed equally to this work.

https://doi.org/10.1016/j.ijmultiphaseflow.2024.104731
Received 26 July 2023; Received in revised form 20 December 2023; Accepted 5 January 2024

breaking. This stochastic process can be explained in two different ways. The first hypothesis suggests that droplets immersed in a turbulent flow break only when interacting with an eddy with sufficient energy to overcome their surface restoring energy (Coulaloglou and Tavlarides, 1977; Karimi and Andersson, 2018). On the other hand, the second hypothesis implies that turbulence excites the droplet surface until a resonance mechanism induces breakup (Risso and Fabre, 1998; Lalanne et al., 2019). Additionally, the breakup of a droplet may result from an interplay between both phenomena.

In recent years, advances in numerical solvers and supercomputer capabilities have facilitated the study of droplet breakup under turbulent flow with direct numerical simulations (DNS). DNS of two-phase flows under turbulent conditions have been studied for various purposes, such as the analysis of the turbulent–interface coupling to develop sub-grid closure models for large eddy simulations (Trontin et al., 2010; Duret et al., 2012; Canu et al., 2018), the investigation of the turbulence–interface coupling in the presence of droplets or bubbles (Dodd and Ferrante, 2016; Roccon et al., 2017; Rosti et al., 2019; Crialesi-Esposito et al., 2022, 2023; Krzeczek et al., 2023), and the estimation of the effect of surfactants or mass transfer on the turbulent–interface coupling (Soligo et al., 2019; Martinez et al., 2023). DNS of single droplet/bubble breakup process has also been of major interest in understanding the underlying mechanisms driving droplet breakup (Qian et al., 2006; Perlekar et al., 2012; Komrakova et al., 2015; Mukherjee et al., 2019; Shao et al., 2018; Karimi and Andersson, 2020; Perrard et al., 2021; Rivière et al., 2021; Vela-Martín and Avila, 2021, 2022; Håkansson et al., 2022; Farsoiya et al., 2023). A notable advantage of studying individual bubble, or droplet, breakup is that the breakup process is independent of the influence of coalescence events between droplets that complexifies the analysis. For a comprehensive overview of previous works on DNS of two-phase flows under turbulent conditions, along with their specific applications, refer to Table 1. An extended version of this Table is presented in Fig. A.8 and given as a tabular in the additional material.

In this communication, we focus on the prediction of neutrally buoyant droplet breakup in turbulent flow by mean of a shape parameter analysis. A database of oscillating droplets under turbulent flow is generated with our in-house multiphase flows DNS solver. The viscous and density ratios are kept constant, and a single Weber number is studied, chosen near the droplet critical Weber number. This enables generating a large number of droplets ensuring that the breakup statistics are converged. This database has previously been used in our work to analyze droplet oscillations (Roa et al., 2023). The latter shows that the oscillations are related to the natural frequency of the droplet and explores the coupling between spherical harmonics modes. The present study, however, focuses on describing the final stages before droplet breakup using several shape parameters. The objective of our work is to assess the capability of these shape parameters to predict the shape evolution of a droplet in a turbulent flow, and provide breakup thresholds to forecast droplet breakage for the studied flow conditions. The present paper is organized as follows. The DNS solver is introduced in Section 2, along with the methodology to perform accurate simulations of a single neutrally buoyant droplet breakup under turbulent flow and the parameters considered to build the droplet breakup database. In Section 3 the shape parameters are defined. Section 4 focuses on the analysis of the database in order to give a qualitative description of the typical temporal evolution of a droplet, , and predict the breakup of a droplet under turbulent flow using shape parameters.

2. Numerical procedure

2.1. Navier–Stokes solver

The present study is realized using our in-house multiphase solver, ARCHER (Ménard et al., 2007; Archer web page, 2023). This DNS solver solves the two-phase incompressible Navier–Stokes equations on a cubic staggered grid with decoupled pressure and velocity. The interface is captured using a coupled level-set volume-of-fluid approach (CLSVoF), accurately describing the geometrical properties of the interface (second-order) through the level-set method while ensuring mass conservation via the volume of fluid method. The combination of level-set and volume-of-fluid fields enables the detailed computation of the primary quantities related to the droplet shape, see Section 3 (see also Chéron et al. (2019)).

The convective terms are solved in a conservative form (Rudman, 1998; Vaudor et al., 2017), the viscous terms are discretized with the Sussman scheme (Sussman et al., 2007), and the pressure jump is treated with a ghost fluid approach (Fedkiw et al., 1999). The temporal integration is performed using a second-order prediction–correction scheme. The in-house Poisson solver relies on the multi-grid gradient conjugate algorithm MGCG (Zhang, 1996).

This solver has been applied to study primary atomization (Lebas et al., 2009), as well as secondary atomization under turbulent conditions (Duret et al., 2012; Canu et al., 2018, 2020).

2.2. Generation of a database

The methodology employed to generate droplet breakup under turbulent flow was initially presented in Chen et al. (2019) and Chéron et al. (2019). Here, the methodology is used to create a database of droplets evolving under turbulent conditions. This database is created by performing multiple realizations of the same physical configuration, the viscous and density ratios are kept constant as well as the turbulent Reynolds and Weber numbers. The overall procedure is illustrated in Fig. 1. Each realization involves three steps:

1. A single-phase turbulent background is generated and maintained in a tri-periodic domain by forcing the energy to a target level throughout the simulation. We apply the linear forcing method based on Rosales and Meneveau (2005), which has been used in our research group for the past decade (Duret et al., 2012; Canu et al., 2018; Martinez et al., 2023). The forced single-phase turbulent flow is held for multiple eddy-turnover times to develop a fully developed homogeneous isotropic turbulent flow.
2. Then, a fixed solid spherical particle is introduced in the computational domain. The no-slip velocity is ensured thanks to the immersed boundary method (Uhlmann, 2005; Breugem, 2012; Chéron, 2020).
3. Once the turbulent flow is statistically stationary and the no-slip velocity boundary condition is accurately enforced at the surface of the fixed solid particle, the solid particle is replaced by a freely moving spherical droplet of the same radius following the methodology of Chéron et al. (2023).

The simulations continue until the breakup of the droplet is detected. The feasibility of long simulations is achieved since there is no mass loss during the simulation, allowing for different realizations with limited numerical cost.

The temporal details of the simulation are the following. Every five eddy-turnover times, the single-phase velocity and pressure fields are recorded (step 1). For each single-phase snapshot, nine different simulations are performed by fixing the solid particle at a different position in the computational domain. Every half eddy-turnover time, the flow field is saved (step 2). A two-phase flow simulation is launched for every snapshot of step 2, and the two-phase flow is saved 25 times per eddy-turnover time (step 3).

The above procedure is carried out to ensure that the initial turbulent condition does not perturb the surface. The results presented in Appendix B discuss the influence of the present methodology to initialize the flow conditions compared to a configuration where the droplet is instantaneously added to a turbulent flow (Crialesi-Esposito et al., 2023; Vela-Martín and Avila, 2022; Håkansson et al., 2022; Håkansson and Brandt, 2022), on the temporal evolution of the droplet

Table 1
Overview of interface resolved DNS of fluid–fluid turbulent flow. Dimensionless numbers are defined in Section 2.3. A visual presentation of all the simulations is given in Appendix A, Fig. A.8 and a readable database of all the previous works is given in the additional material. For emulsions studies, the volume fraction, ϕ, defined as the fraction between the dispersed and the total volume, is given. Unless otherwise stated, Weber numbers correspond to $We = 2.3 \times \frac{\rho_c \epsilon^{2/3} D^{5/3}}{\sigma}$.

References	Numerical approach	Turbulence and IC	Re_λ	We	$\frac{\rho_d}{\rho_c}$	$\frac{\mu_d}{\mu_c}$	Comments	Main results
Crialesi-Esposito et al. (2022, 2023)	VoF	Sustained HIT. One droplet	137	21.2–106.5	1	0.01–100	$\phi = 0.03$–0.5	Droplet distribution. Assessment of Hinze parameter
Dodd and Ferrante (2016)	VoF	Decaying HIT. Several droplets	83	0.1–5[a]	1–100	1–100	$\phi = 0.05$	Turbulence kinetic energy exchange droplet. Energy transfers. Breakup/Coalescence rate. Droplet shape and surface
Duret et al. (2012), Canu et al. (2018) and Martinez et al. (2023)	CLSVoF	Sustained HIT. 8 droplets	23	30[b]	30	30	$\phi =$ 0.01–0.95	Total surface. Emulsion. Evaporation rate. Curvature study. Vaporization and curvature coupling
Farsoiya et al. (2023)	VoF	Sustained HIT. One droplet	38–77	1.3–34.5	1	0.01–350	–	Breakup statistics: breakup rate, daughter size. Parametric study
Håkansson et al. (2022) and Håkansson and Brandt (2022)	VoF	Sustained HIT. One droplet	33	1.15–69	0.9	22	–	Droplet/eddy interaction. Droplet shape and surface
Komrakova et al. (2015)	LBM	Sustained HIT. One droplet	24–141	NA	1	0.3−1	Ca = 0.001–0.1	Number of droplets. Energy spectra.
Krzeczek et al. (2023)	VoF	Decaying HIT with gravity. Several droplets	104	0.1	0.9–1.6	0.9–1.6	$\phi = 0.125$	Study of segregation due to gravity
Mukherjee et al. (2019)	LBM	Sustained HIT. One Droplet	30–118	0.03–0.22[c]	1	1	$\phi =$ 0.01–0.45	Droplet distribution. Energy transfers. Emulsion study
Perlekar et al. (2012)	LBM	Sustained HIT. Some droplets	47.4–94.9	1.2–4.3	1	1	$\phi =$ 0.0007–0.09	Energy transfers. Droplet size distribution. Surface evolution. Assessment of Hinze parameter and local Weber number
Qian et al. (2006)	LBM	Sustained HIT. One droplet	14.6–35.8	0.6–5.3[d]	1	1	–	Breakup dynamics.
Rivière et al. (2021) and Perrard et al. (2021)	VoF	Sustained HIT. One bubble	38	3.4–51.7	0.00357	0.04	–	Bubble deformation Sub-Hinze bubbles. Energy transfers. Bubble size distribution.
Roccon et al. (2017)	Cahn–Hilliard	Wall bounded turbulence. Several droplets	150[e]	0.75–3[e]	1	0.01–100	$\phi = 0.18$	Breakup rate. Turbulence modulation.
Rosti et al. (2019)	VoF	Shear turbulence. Several droplets	83–142	0.2–5[f]	1	1	$\phi = 0.05$	Turbulence kinetic energy study. Droplet distribution
Shao et al. (2018)	Levelset	Sustained HIT. One droplet	104	10–55.6[d]	1	1	–	Vortical structures alignment around interface
Soligo et al. (2019)	Phase-field	Wall bounded turbulence. 256 droplets	300[e]	1.5–3[e]	1	1	–	Breakup rate. Surfactants distribution.

(continued on next page)

shape. The strategy to initialize DNS of single droplets in turbulent flow affects the initial growth of the shape deformation. The results show that the present method avoids the initial corrugations observed among others by Crialesi-Esposito et al. (2023, Fig. 3a) and Komrakova et al. (2015). For bubbles, the velocity can be initialized to zero inside the bubble (Rivière et al., 2021; Perrard et al., 2021). However, this approach cannot be applied in the context of this study since the volume fraction and the density of the disperse phase is not negligible. Out of a total of 260 breakup events, 68 degenerated cases have been excluded resulting in a database of 192 realizations and 389,478 snapshots. Those degenerated cases will be discussed in the next Section.

This database, or a part of it, has already been analyzed in the study of the transformation criteria for Lagrangian–Eulerian hybrid methods (Chéron et al., 2019, 2023), the investigation of the 2D projection on shape parameters (Chéron et al., 2022), and the analysis of droplet oscillations (Roa et al., 2023).

2.3. Physical and numerical parameters

The physical and numerical parameters chosen to build the database of droplet breakup under turbulent flow are subjected to three constraints.

Firstly, as the main goal of our study is to perform numerous realizations to generate a large database, the numerical cost of each

Table 1 (*continued*).

Trontin et al. (2010)	Levelset	Decaying HIT. Planar sheet	74	0.2–110 [g]	1	1	$\phi = 0.05$	Energy transfers. Final droplet distribution
Vela-Martín and Avila (2021, 2022)	Cahn–Hilliard	Sustained HIT. One droplet	31–96	3.3–16.7	1	0.5–2	–	Droplet/eddy interaction. Energy transfers. Breakup rate. Stochastic model.
Present study and Roa et al. (2023)	CLSVoF	Sustained HIT. One droplet	40	3.22	1	1	–	– Droplet oscillations

Notes:

[a] $We = \frac{\rho_c u'^2 D}{\sigma}$.

[b] $We = \frac{\rho_d u'^2 L}{\sigma}$, where L is the domain length.

[c] $We = 2.3 \times \frac{\rho_c \epsilon^{2/3} L^{5/3}}{\sigma}$ where L is the domain length.

[d] $We = \frac{\rho_d (\delta u')^2 D}{\sigma}$, where $\delta u'$ is the velocity fluctuation in a distance equal to the droplet size.

[e] Dimensionless numbers based on the shear, $Re = \frac{\rho_c u_\tau h}{\mu_c}$, $We = \frac{\rho_c u_\tau^2 h}{\sigma}$, where u_τ is the shear velocity and h the channel height.

[f] $We = \frac{\rho_c S^2 D^3}{\sigma}$, where S is the uniform mean shear.

[g] $We = \frac{\rho_d u'^2 \delta}{\sigma}$, where δ is the initial sheet thickness.

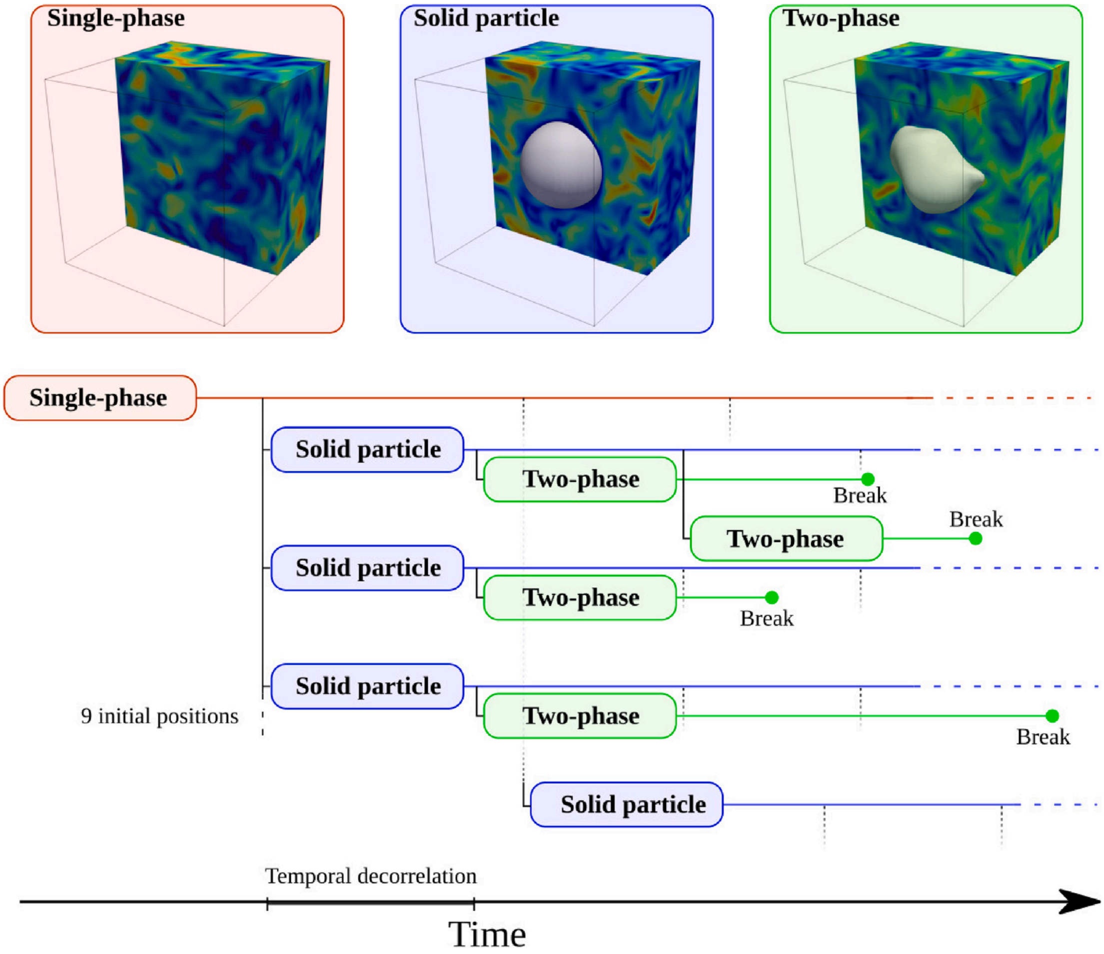

Fig. 1. Droplet database numerical procedure.

simulation must be as small as possible. The number of Eulerian fluid cells is set to 64^3. The constraint on the numerical cost should be fixed, taking into account the minimal mesh refinement needed to correctly reproduce the breakup mechanism. The droplet diameter is fixed at $D = 30\ \Delta x$, where Δx represents the Eulerian fluid mesh size, as determined from our previous studies (Chéron et al., 2019). To balance computational efficiency and accuracy, a domain size of $L = 2.14\ D$ is selected. However, this numerical configuration favors the appearance of non-isolated droplets that can touch each other across the periodic domain. Such degenerated cases occurred 68 times and, as previously mentioned, have been removed from the database.

A second drawback of the confined domain is that the turbulence is not completely developed, leading to another restriction: a finer Eulerian fluid mesh is necessary to separate the Kolmogorov and the integral length scales (Pope, 2000, Equation 9.7). As mentioned in Section 2, the linear forcing of Rosales and Meneveau (2005) and Duret et al. (2012) has been applied. This forcing has been used for a total of 64^3 Eulerian fluid cells in previous works, and encourages us to use it even at a low Reynolds number, i.e., $Re_\lambda \simeq 40$. Here, the Reynolds number is defined as $Re_\lambda = \frac{\rho_c \lambda u'}{\nu_c}$, where λ is the Taylor length scale ($\lambda = \sqrt{\frac{15\mu_c u'^2}{\rho_c \epsilon}}$), ρ_c is the carrier fluid density, μ_c is the carrier fluid kinematic viscosity, ϵ is the average dissipation rate, and u' is the turbulent velocity fluctuations. Density and viscosity ratios, $\frac{\rho_d}{\rho_c}$ and $\frac{\mu_d}{\mu_c}$ respectively, are set to unity, as the forcing shows non-physical behavior for the same configuration with a density ratio larger than one, resulting in an increase in the droplet angular velocity during the first eddy-turnover time. Aniszewski and Brändle de Motta (2022).

Finally, this paper focuses on the study of the sub-Hinze droplets breakup. Hence, the surface tension is determined by the Weber number, here set to $We = 0.9$, where $We = \frac{\rho_c u'^2 D}{\sigma}$, σ being the surface tension. For this choice of Weber number, we can determine the supposedly maximum droplet diameter that does not undergo breakup by calculating the Hinze scale (Hinze, 1955; Perlekar et al., 2012) $d_{\mathrm{H}} = 0.725 \left(\frac{\rho_c}{\sigma}\right)^{-3/5} \epsilon^{-2/5}$, which is equal to $d_{\mathrm{H}} = 0.6D$. For density and viscosity ratios set to unity, the Weber number is a very sensitive parameter to vary for analyzing droplet breakup, and must be chosen adequately to observe droplet oscillation before breakup. Values lower than the critical Weber number yield to excessively long-time simulations before breakup, whereas for Weber numbers larger than the critical Weber number, the breakup of the droplet occurs during the first droplet's shape deformation (Vela-Martín and Avila, 2022). However, the given value of the surface tension yields to turbulent and capillary times of the same order of magnitude which makes difficult to differentiate interface-driven and turbulent-driven phenomena.

Here, the Weber number is proportional to the square of the ratio between the capillary time ($t_c = \sqrt{\frac{\rho_c D^3}{8\sigma}}$), and the turbulent time ($t_t = \frac{D}{u'}$). Some authors also define the Weber number by considering the eddy velocity equivalent to the size of the droplet diameter D. Based on the Kolmogorov–Hinze assumption for fully developed turbulent flows (Ni, 2024; Kolmogorov, 1949; Hinze, 1955), the corresponding Weber number value is $We_{KH} = 2.3 \times \frac{\rho_c \epsilon^{2/3} D^{5/3}}{\sigma} = 3.22$. This Weber number is based on the turbulent inertial time at the characteristic length of the droplet ($t_{inertia} = \left(\frac{D^2}{\epsilon}\right)^{1/3}$). Time is normalized using the capillary time with $t_{inertia} = 2.41\ t_c$.

The Kolmogorov–Hinze Weber number is based on the assumption that $\langle(\delta u')^2\rangle(D) \simeq (\epsilon D)^2/3$. When dealing with numerical simulations at moderate Reynolds numbers, this assumption does not hold (see for example Qian et al., 2006). The numerical dissipation, the forcing scheme or the domain to droplet length ratio can strongly modify two-point velocity correlations. Thus the comparison of results with studies of similar We_{KH} is not straightforward.

3. Definition of the shape parameters

The shape parameters employed in this numerical study, and defined in this Section, are based solely on primary quantities, as illustrated in Fig. 2. These parameters include the maximum and minimum distances from the center of mass of the droplet, denoted as a and b respectively, the equivalent radius R based on the total volume of the droplet ($V = \frac{4}{3}\pi R^3$), the total surface area of the droplet S, and the volume of the intersection between the equivalent sphere and the entire droplet ($V_{S\cap D}$). Additionally, local mean and Gaussian curvatures, computed from the two main curvatures $H = \frac{1}{2}\left(\kappa_1 + \kappa_2\right)$ and $G = \kappa_1\kappa_2$, provide further information for characterizing the morphology of a set of droplets (Canu et al., 2018). These quantities lead to the definition of seven different parameters that characterize the shape of the droplets in the database. Table 2 provides the names, mathematical expressions, and boundary limits of each shape parameter as given in the literature. The computation of primary quantities and associated shape parameters is performed using our in-house post-processing tool, PyArcher (Archer web page, 2023). For curvature-based quantities, PyArcher utilizes algorithms described by Mohamed et al. (2019) and Battista et al. (2019), which are also present in the Mercur(v)e project (Mercur(v)e web page, 2023). Many of these parameters were thoroughly studied in our previous work (Chéron et al., 2022).

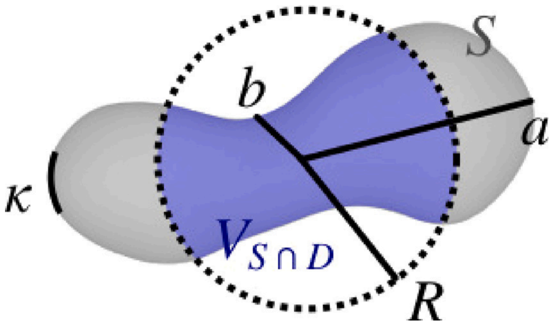

Fig. 2. Primary quantities used to define the shape parameters.

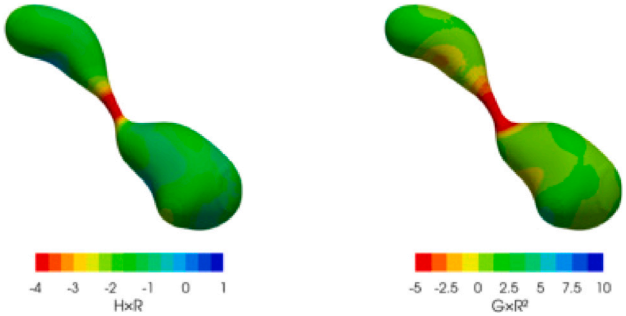

Fig. 3. Dimensionless mean (left) and Gaussian (right) local curvature of the droplet given in Fig. 4 at time $t = 45.91\ t_c$. A video with the temporal evolution of this Figure is given in the additional material.

In Table 2, two shape parameters are computed using the local curvature at the droplet's interface. The curvature provides valuable information about the atomization process, even for complex topologies such as emulsions with large volume fractions (Canu et al., 2018; Henry and Tegze, 2019). The scatter plot of the mean and Gaussian curvatures, $H - G$, is analyzed throughout the entire database, but for the present discussion, we focus on two main criteria based on the curvature.

The first criterion is the average mean curvature (Mohamed et al., 2019; Chéron et al., 2019). The second criterion is based on the parameter proposed by Håkansson et al. (2022), which is defined as the average of the smallest 10% of the Gaussian curvature values, and here referred to as G_{min}. For a spherical droplet of Gaussian curvature $1/R^2$, the parameter G_{min} is equal to 1.[2]

The surface mean and Gaussian curvature for the droplet shown in Fig. 4 before breakup is depicted in Fig. 3. As indicated by the red color in Fig. 3 (right), the ligament present in the late stages preceding the breakup is characterized by negative Gaussian curvature. This observation provides important insights into the breakup mechanism and explains the interest of the parameter G_{min}.

4. Results

4.1. Qualitative description

To illustrate the temporal evolution of the droplet shape in a turbulent flow until breakup, several successive snapshots of the interface

---

[2] There is an inconsistency in the values in Håkansson et al. (2022, Fig. 6) since the initial shape is a sphere and the initial values in the figure are around minus 4. The corresponding author confirm us this inconsistency and found a new methodology to correct the issue.

Table 2
Shape parameters definition. The bound corresponding to a sphere is in bold. These parameters are often derived from their equivalent in two dimensions (see references column).

Name	Definition	Bounds	References
Aspect ratio	$\alpha = \frac{b}{a}$	$[0, \mathbf{1}]$	Adrian (1991) and Masuk et al. (2021)
Uniformity	$\eta = \frac{a-b}{R}$	$[\mathbf{0}, \infty)$	Blaisot and Yon (2005)
Maximal deformation	$\hat{a} = \frac{a-R}{R}$	$[\mathbf{0}, \infty)$	Lalanne et al. (2019), Masuk et al. (2021) and Qi et al. (2023)[a]
Irregularity	$\iota = 4\pi \frac{R^2}{S}$	$[0, \mathbf{1}]$	Podczeck et al. (1999)
Symmetric difference	$\psi = 2\frac{V-V_{S\cap D}}{V}$	$[\mathbf{0}, 2]$	Malot and Blaisot (2000) and Chéron et al. (2022)
Curvature	$\tilde{H} = R\langle H \rangle_{\Sigma}$	$(-\infty,$ unknown$]$ (Sphere: $-\mathbf{1}$)	Chéron et al. (2019)
Minimal Gaussian	$G_{min} = R^2 \langle G \rangle_{G<P_{10\%}(G)}$	$(-\infty, \mathbf{1}]$	Håkansson et al. (2022)

Notes:
[a] Qi et al. (2023) calls $\frac{a}{R}$ the aspect ratio.

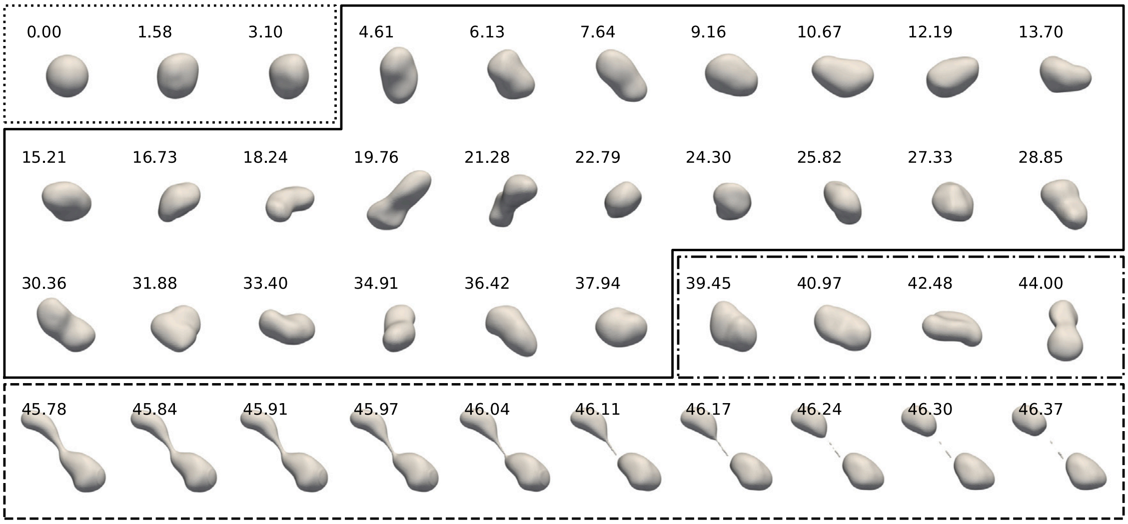

Fig. 4. Temporal evolution of a droplet interface. Time is given dimensionless (t/t_c). Initial deformation (dotted line), oscillatory regime (solid line), no-return deformation (dash-dotted line) and capillary driven breakup (dashed line, the time between two snapshots is reduced). The corresponding video is included in the additional material.

of a droplet extracted from the database are shown in Fig. 4. From the initialization to the breakup of the droplet, four stages of deformation are observed:

1. During the very first capillary times, the droplet undergoes an initial deformation (see the three first snapshots in Fig. 4). Because of the specific initialization procedure, in which the droplet velocity is set to zero and the no-slip velocity is enforced at the surface of the solid particle, this first step is slower than in other publications, see Appendix B. Roa et al. (2023) and Perrard et al. (2021)).
2. Then, the droplet oscillates during several capillary times. The study of these oscillations is beyond the scope of the present communication and has been extensively analyzed in Roa et al. (2023). During these oscillations, strong deformations can be observed (see for instance snapshot at $t = 19.69\ t_c$ in Fig. 4).
3. Before breakup, the droplet undergoes a critical deformation which yields to a no return deformation state for the droplet. The characterization of this initial deformation and the time to reach the final breakup is the main purpose of the present study (see in particular Section 4.2). The use of shape parameters helps detect this critical deformation, and thus to predict the incoming breakup.
4. Finally, as mentioned by Håkansson et al. (2022), a ligament is generated between two lobes in a critical deformed state characterized by the capillary instability (Rayleigh–Plateau). This accelerates the breakup process. The instabilities can be observed in the last row of Fig. 4, where the time step is adapted to accurately observe the phenomenon. This process has been studied in previous works and is responsible for the generation of satellite droplets resulting from the breakage of the ligament (Stone, 1994; Villermaux, 2020; Rivière et al., 2022; Qi et al., 2023).

These four stages are observed for all the droplets in the database. The breakup times of these droplets vary in the range $t_{break} = 9.09\ t_c$, to a maximum breakup time of $t_{break} = 376\ t_c$. The study of the time spent before breakup is analyzed in Appendix C.

These main stages of the droplet breakup under turbulent flow are commonly found in the literature. A recent analysis of the duration of each stage has been carried out by Qi et al. (2023).

4.2. Breakup analysis using shape parameters

Many authors have attempted to predict the breakup of droplets and bubbles under turbulent flow using a cut-off shape parameter (Perlekar et al., 2012; Lalanne et al., 2019; Håkansson et al., 2022; Qi et al., 2023). Describing droplet deformation based on a given shape parameter is common in the literature, but it has not led to a consensus on the key shape parameters to consider (Ghaemi et al., 2009; Chéron et al., 2022). This complexity arises from the fact that droplet deformation cannot be fully captured by a simple scalar value. In this study, we perform a multidimensional analysis of the droplet breakup by analyzing the evolution of various existing shape parameters, given in Section 3, until droplet breakage.

4.2.1. Temporal evolution of the shape parameters

In Fig. 5, we present the temporal evolution of all the aforementioned shape parameters for the droplet shown in Fig. 4. The three stages described in Section 4.1 can be identified: (1) initial perturbation growth of the deformation for $t < 4\ t_c$; (2) shape oscillations of the droplet during several capillary times with a strong deformation at $t \simeq 20\ t_c$; and (3) large deformation of the shape of the droplet with changes in shape parameters at $t > 40\ t_c$. The delimitation of those stages are arbitrarily chosen from qualitative analysis because they are challenging to define precisely.

The strong deformation observed at $20\ t_c$ highlights the complexity of understanding the dynamics leading to breakup and indicates that a comprehensive understanding might require additional factors beyond shape parameters alone.

The different shape parameters do not exhibit a similar temporal evolution. First, the initial deformation occurring at $t < 4\ t_c$ is not visible for the curvature shape parameter $\tilde{H}$, and the oscillations are less pronounced with this parameter. Secondly, the duration of strong deformation leading to the breakup cannot be identified identically for all parameters. For parameters α to ψ, this deformation begins at approximately $t = 40\ t_c$, while it seems to start at approximately $t = 42\ t_c$ for curvature-based parameters.

For η and $\hat{a}$, which are similar in their definitions based on primary lengths, the final deformation is represented by a monotone increase in the shape parameter. A similar increase before breakup is observed experimentally by Qi et al. (2023) for bubbles in turbulent flow. The same trend is observed with the symmetric difference shape parameter, ψ, which is suitable for accounting for the typical breakup between two droplets connected by a neck (Håkansson et al., 2022). In this case, the intersection of the volume of the droplet and the equivalent sphere, $V_{S\cap D}$ tends to zero since the equivalent sphere, S, is only an intersection of the remaining ligament.

However, the aspect ratio parameter, α, and the shape parameter proposed by Håkansson et al. (2022), G_{min}, are not able to predict the breakup for this specific realization. The values during this breakup sequence ($t > 40\ t_c$) are close to the values observed for the strong deformations at approximately $20\ t_c$. For instance, the shape parameter G_{min} reaches a plateau for the elongation observed at approximately $t \simeq 20\ t_c$. As the neck radius becomes small, the minimum value of the Gaussian curvature is limited, resulting in a plateau. After this plateau, G_{min} decreases, which could serve as a good criterion to define the time transition between stage (3) and (4).

The uniformity and maximal deformation shape parameters also show a shift in their temporal evolutions during this last stage. These observations provide valuable insights into the droplet breakup process and highlight the differences among the various shape parameters in characterizing the deformation and breakup of droplets under turbulent flow conditions.

To go further into the analysis, we conduct a statistical study by representing 50,000 snapshots of the two-fluid flow from our database in terms of their shape parameters in Fig. 6 (a complete scatter plot of the database is provided in Appendix A). Each shape parameter (except for the aspect ratio) is plotted as a function of the aspect ratio, with each point representing the state of a droplet at a specific time in the simulation. The color bar indicates the remaining time before the droplet breaks, $t - t_{break}$, where $t - t_{break} = 0$ indicates the droplet breakup. The points located at $\alpha = 1$ correspond to the initial time of the simulations, depicting a perfect sphere. This state is never recovered during the droplet lifetime.

Additionally, Fig. 6 provides the values of each shape parameter for specific cases of an oblate and a prolate spheroid. These correlations have been analytically derived in previous works by Blaisot and Yon (2005) and Chéron et al. (2022). For curvature-based shape parameters, the correlations have been computed numerically using our post-processing procedure from synthetic spheroids. These statistical analyses provide valuable insights into the relationships between different shape parameters and their influence on droplet deformation and breakup in turbulent flow conditions. As expected, the scatter plot between the aspect ratio and each individual shape parameter yields different results. We have previously analyzed the complexity of the shape parameters in our earlier work (Chéron et al., 2022). The similar evolution for the database droplets with the correlation for perfect spheroids indicates that the droplets' deformation follows a specific trend: the droplets experience significant deformations and exhibit no local corrugations. This observation is further supported by the spherical harmonics decomposition analysis carried out in the study of Roa et al. (2023). Note that the minimal Gaussian criteria, G_{min}, deviates from the spheroidal trend since for a spheroid, the Gaussian curvature is always positive, and G_{min} is designed to monitor negative Gaussian curvature values. As for $\tilde{H}$, the average mean curvature is consistently close to -1, representing a perfect sphere, and only decreases for large deformation values.

Some points near the breakup (shown in red) display non-physical behavior. These points correspond to distorted shapes that can arise before the actual breakup occurs. Additionally, this plot reveals the common dynamics of the breakup shared by all the droplets. (i) For long times, predicting the exact moment of breakup is not feasible. (ii) However, for all the shape parameters, large deformations are indicative of an imminent breakup.

4.2.2. *Breakup prediction from shape parameters*

Fig. 7 (top row) shows the histogram of each shape parameter for droplets breaking in the next $0.5\ t_c$, as well as the overall histogram of the whole database.

The comparison between the two histograms confirms that droplets with an upcoming breakup event have more probability to undergo large deformations. That conveys the simple idea that a droplet is strongly deformed before breakup. This observation is true for all the shape parameters.

For each shape parameter, a threshold can be defined to predict the majority of drops that will break (true positives) while minimizing the number of drops that will not break (false negatives). This threshold is the one whose ensures the best *area under the curve* (AUC) score, and is plotted as a vertical line in Fig. 7.

The AUC score has been selected for its ability to be a good criterion for unbalanced classification problem. The critical threshold values for each parameter, with the AUC score associated, are given in Table 3. The higher the score, the better it is at predicting breakup events. In particular, the G_{min} criteria is notably the worst while $\tilde{H}$ is somewhat better than the others. No AUC scores are reaching the ideal value of 1, meaning that none of those are perfect predictors. As an example, the strong deformation observed around $20\ t_c$ for the realization given in Fig. 5 is wrongly predicted as a breakup event by all these thresholds.

The threshold values given are also in agreement with the literature, even for totally different configurations. In Lalanne et al. (2019), a critical value of $\hat{a} = 1$ is obtained with a different methodology. For Qian et al. (2006) and Perlekar et al. (2012), the breakup occurs for S^* below 0.35 (see Perlekar et al. (2012, Figure 5) and Qian et al. (2006, table V).) which corresponds to ι above 0.75. For Håkansson et al. (2022), the critical values of the criterion $A/A_0 = 1/\iota$ are 1.3 and 1.6, corresponding to values of the irregularity between 0.6 and 0.7.

The universality of these thresholds may indicate that the breakup process occurs in a similar manner regardless of the properties of the two fluids considered in each configuration. Indeed, the triggering of capillary process, that drives the final stages of the breakup process, is more related to the shape of the deformed droplet/bubble than to the physical parameters. The physical parameters provide more information about the duration of the no-return state: the statistical average time to reach the critical shape is given by the Weber number (see Appendix C and Vela-Martín and Avila (2022)), and the duration of the final stage in which breakup is driven by capillary, inertia and viscosity. This later stage is related to the time to break the neck, that explains the long times spent by the droplets studied by Håkansson et al. (2022) in a more viscous case, or the long ligaments observed by different authors (Eastwood et al., 2004; Farsoiya et al., 2023).

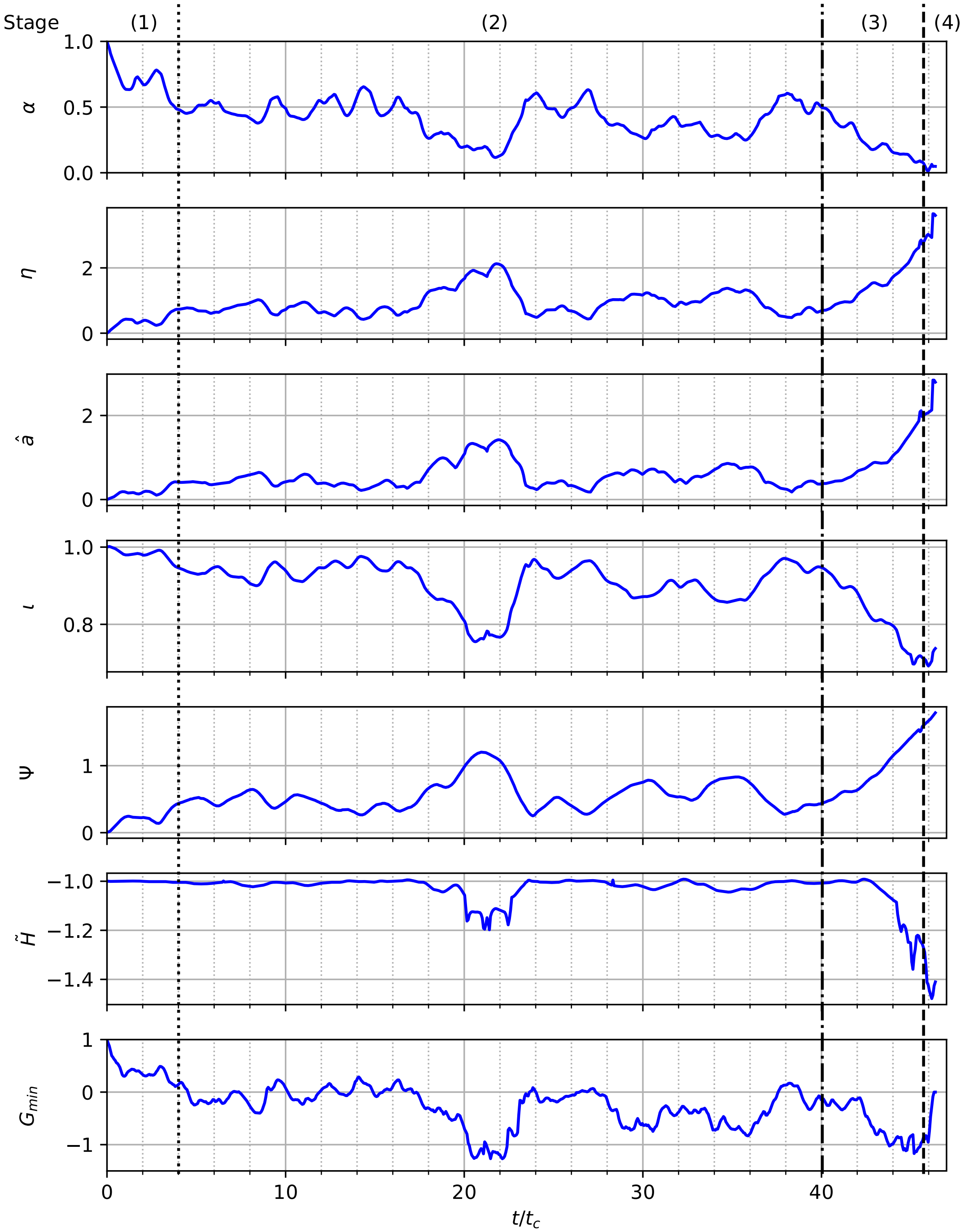

Fig. 5. Shape parameters temporal evolution of the realization given in Fig. 4. Vertical lines correspond to the transition between the stages described in Section 4.1. The primary quantities of this droplet are given in the additional material.

Table 3
Values of the critical threshold value, the AUC score for each parameter for a breakup occurring in the next 0.5 t_c.

Name	Symbol	Threshold	AUC score
Aspect ratio	α	0.19	0.97
Uniformity	η	1.90	0.98
Maximal deformation	$\hat{a}$	1.11	0.97
Irregularity	ι	0.78	0.98
Symmetric difference	ψ	1.16	0.98
Curvature	$\tilde{H}$	−1.16	0.99
Minimal Gaussian	G_{min}	−0.55	0.78

To study the temporal behavior, Fig. 7 (bottom) provides the time evolution of the probability density function of each parameter before breakup . For $t_{break} - t = 0.5\ t_c$ the colors correspond to the top row blue histogram. For large times ($t_{break} - t > 10\ t_c$), the histogram corresponds to that of the entire database, representing the averaged deformation of droplets under turbulent conditions (black histogram of the top row). For $t_c < t_{break} - t < 10\ t_c$, the shape parameters exhibit an increase in shape deformation (histograms shift from averaged deformation to strong deformation). This increase of the shape parameters is similar to the observations shown for a single droplet in Fig. 5 and also for averaged maximal deformation parameter by Qi et al. (2023).

The AUC scores and thresholds are also provided for each time interval. For times in range $t - t_{break} > 10\ t_c$, accurate predictions are not

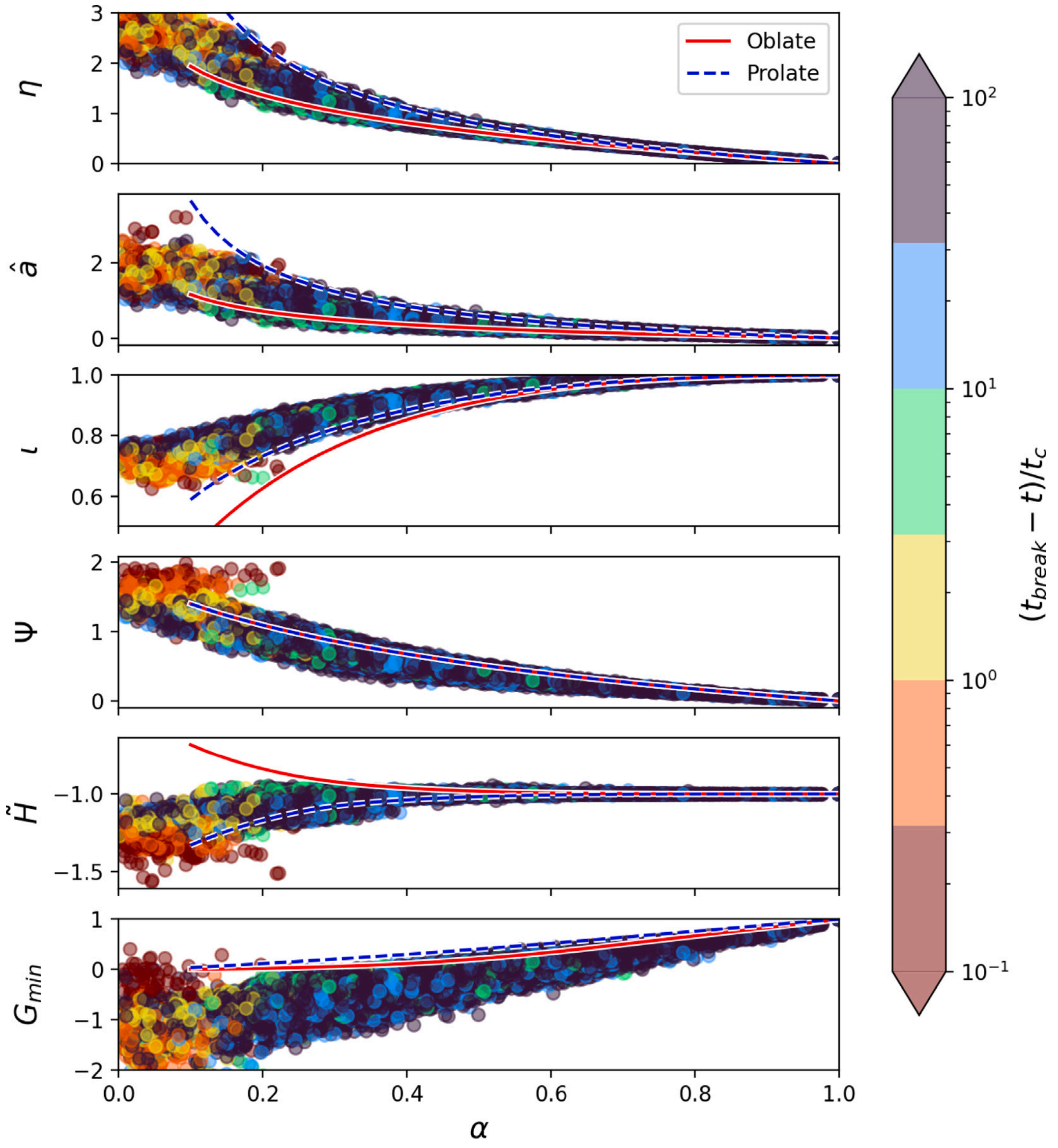

Fig. 6. Scatter plot of shape parameters as a function of the aspect ratio. Color by time remaining before break. The lines represent the case of oblate (solid red) and prolate (dashed blue) spheroids. A complete version of this figure is given in Appendix A, Fig. A.9.

possible as indicated by the low AUC score of all the shape parameters. For times in the range $t_c < t_{break} - t < 10\ t_c$, the AUC score increases for all the parameters until reaching a maximum at $t_{break} - t \simeq t_c$. However, notable differences are observed between the curvature based shape parameters and the remaining ones for near breakup times. For the latter parameters, α, η, $\hat{a}$, ι, ψ, a similar behavior is observed for times in the range $t_{break} - t > t_c$; the AUC score indicates good prediction ability, and the threshold criteria remain constant and close to that of $t_{break} - t = 0.5\ t_c$, as shown in Table 3 and the top Fig. 7. The other criteria based on curvature behave differently. For instance, the AUC score associated to the threshold for the average mean curvature, $\tilde{K}$, shows the best breakup prediction ability for times close to breakup time compared to the parameters α, η, $\hat{a}$, ι, ψ, which is consistent with the observation in Fig. 5. For the shape parameter, G_{min}, after reaching a local minimum at approximately $t \approx t_c$, the breakup threshold value increases for the near breakup time which reduces the AUC score associated to the threshold value of the parameter. This phenomenon is caused by the reduction of the neck diameter, as also observed in Fig. 5.

In summary, the study of these parameters reveals the following: for a time before the breakup greater than 10 t_c, the breakup process is not engaged. Then, at $t_{break} - t \simeq 10\ t_c$, the process initiates, leading to an increase in the droplet shape deformation. However, the shape parameters do not allow for distinguishing between a strong deformation during oscillations and a critical deformation at this point (the AUC score is below 0.8). Finally, at $t_{break} - t \simeq t_c$, the critical deformation is reached, and the breakup is described by the classical interfacial instability. This process aligns with the description provided in Section 4.1.

In this study the viscous and density ratios as well as the turbulent intensity are constant, which does not enable a parametric dimensional analysis. Nevertheless, to the authors understanding, the two stages before the breakup are driven by two different phenomena. The time spent between the initial deformation and the acceleration due to capillary, stage (3), is 9 t_c, that corresponds to 10 t_c minus the time spent in stage (4). Since the deformation of the droplet is a result of a balance between the surface tension and the surrounding fluid, it seems coherent to relate this time to the natural frequency of the droplet oscillations (Roa et al., 2023). For the time spent in stage (4), the present study itself does not allow to conclude. A study involving shape parameters tailored for characterizing this specific final deformation stage is required, as done by Håkansson et al. (2022). Rivière et al. (2022) suggest that the time spent in stage (4) is linked to the

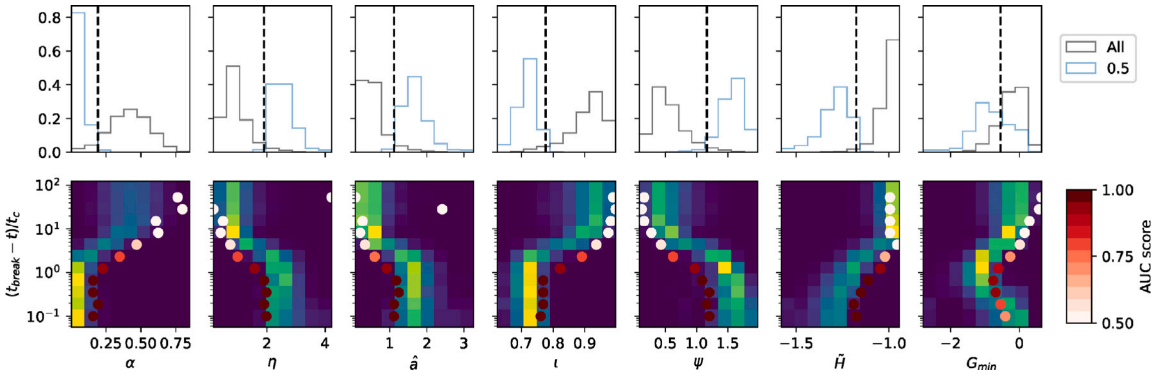

Fig. 7. Probability density function (pdf) of each parameter. Top row, normalized pdf for all the database (black) and for droplets that will break in the next $0.5t_c$ (blue). Bottom row, normalized pdf for droplets as a function of time before breakup (each row, corresponding to a given time, is normalized).

Rayleigh–Plateau instability. This hypothesis potentially explains the long ligaments observed before droplet breakup by Eastwood et al. (2004), Håkansson et al. (2022) and Farsoiya et al. (2023) for large viscosity studies.

Future works with parametric studies are needed to confirm the scaling of the duration of each stage while considering physical pair of fluids. The study of Qi et al. (2023) goes in this direction. Depending on the pair of fluids considered, the behavior can be completely different and depends on the balance between inertial, viscous and capillary forces. To allow a complete description of these latter stages, it is necessary to consider the capillary regime until reaching molecular length scales (Lister and Stone, 1998). The simulations of turbulence induced breakup does not reach this level of accuracy.

5. Conclusion

In the present work, we conducted a comprehensive analysis of a database of droplets oscillating under turbulent conditions, where the density and viscosity ratios were set to unity. The moderate turbulent Reynolds number and Weber number resulted in long hold-up times before breakage. The focus of the study was on the analysis of the breakup process after several oscillations using several shape parameters. For the studied flow configuration, we observe that the breakup process of a droplet can be described by a set of four stages: (1) initial deformation, related to the numerical initial condition; (2) shape oscillations during long times; (3) beginning of a strong deformation; and (4) Rayleigh–Plateau instability causing the final breakup.

The shape oscillations were found to be related to the natural frequency of the droplets (Risso and Fabre, 1998; Roa et al., 2023). Notably, one particular oscillation generates a critical deformation leading to the final breakup of the droplet (Håkansson et al., 2022). The probability of reaching this critical deformation is inversely proportional to the Weber number, We_{KH} (Coulaloglou and Tavlarides, 1977; Vela-Martín and Avila, 2022). However, the mechanisms driving this specific event require further investigation for a deeper understanding. Future work should explore whether it is the result of energy transfer from a large eddy overcoming the restoring surface energy of the droplet or induced by resonant mechanisms.

The analysis of breakup event statistics decoupled from other mechanisms helped to distinguish between the last two stages. The use of shape parameters, provided valuable insights. For each shape parameter a threshold were found to provide the better prediction of the incoming breakup. These thresholds are in agreement with previous literature (Lalanne et al., 2019; Qian et al., 2006; Perlekar et al., 2012). Particularly, as proposed by Håkansson et al. (2022), the minimal curvature-based shape parameters provides additional information about the neck that characterizes the final stage.

Further analysis involving other approaches to describe the interface, such as the Minkowski functionals (Dumouchel et al., 2017, 2022), spherical harmonics (Perrard et al., 2021; Roa et al., 2023), or the scatter plot of mean and Gaussian curvatures ($H - G$) (Canu et al., 2018; Henry and Tegze, 2019), could offer more details on the physics of breakup.

Additional information on the breakup process can be obtained by studying the flow characteristics inside and around the droplet, as suggested by several authors (Qian et al., 2006; Perlekar et al., 2012; Komrakova et al., 2015; Masuk et al., 2021; Qi et al., 2022; Vela-Martín and Avila, 2021). Understanding the effect of turbulence on the initialization of the breakup process and the transition from the oscillatory regime to the breakup stage requires detailed flow analysis.

The scaling of each stage of the sequence should also be clarified. Global breakup statistics have been analyzed in previous studies (Vela-Martín and Avila, 2022; Farsoiya et al., 2023), providing insights into the influence of different parameters such as Weber number, density, or viscosity ratios. Understanding the duration of the oscillatory regime, deformation regime, and final capillary driven breakup is crucial for developing population balance breakup models (Håkansson, 2020). However, the study of the last stage must consider the balance between inertial, viscous, and capillary forces at the final state before breakup and work with realistic fluids and their related molecular sizes.

For the future, it would be necessary to study in detail the effect of different dimensionless numbers. Also, the definition of the appropriate Weber number should be thoroughly discussed, in particular for numerical studies where the Kolmogorov's assumption is not held.

CRediT authorship contribution statement

Camille Deberne: Data curation, Investigation, Writing – original draft, Writing – review & editing. **Victor Chéron:** Methodology, Writing – original draft, Writing – review & editing. **Alexandre Poux:** Resources, Software, Writing – review & editing. **Jorge César Brändle de Motta:** Data curation, Funding acquisition, Software, Supervision, Writing – original draft, Writing – review & editing.

Declaration of competing interest

The authors declare the following financial interests/personal relationships which may be considered as potential competing interests: Jorge César Brändle de Motta reports financial support was provided by French National Research Agency. Jorge Cesar Brandle de Motta reports financial support was provided by Normandy Region.

Data availability

Data will be made available on request.

Acknowledgments

This work was granted access to the HPC resources of IDRIS, TGCC and CINES under the allocation A0132B1010 made by GENCI (Grand Equipement National de Calcul Intensif), France and the CRIANN (Centre Régional Informatique et d'Applications Numériques de Normandie) under the scientific project N. 201 704. The authors would like to thank the Normandy region for their funding of this research, in particular the AMCAS project, as well as the Agence National de la Recherche (ANR), France for their funding of the DropBreak project, ANR-20-CE46-0002.

Appendix A. Extended figures

This Section contains two extended figures. They have not been implemented in the text to improve readability.

Appendix B. Sensitivity of the droplet oscillation to the initial velocity condition in turbulent flow

In Section 2.2 the specific methodology to initialize a simulation of a freely moving droplet in a pseudo turbulent flow is discussed. Here, we compare the methodology developed in this work to the commonly used method which consists of instantaneously adding a droplet to an already developed turbulent flow (Crialesi-Esposito et al., 2023; Vela-Martín and Avila, 2022; Håkansson et al., 2022; Håkansson and Brandt, 2022). With the latter method, there is no initial no-slip condition, so the fluid is not yet adapted to the presence of the droplet which yields to a larger stress. To illustrate the differences between these two methods, we have performed ten simulations where the droplet is instantaneously added to the turbulent flow, and compared the results with the droplets from the database, see Section 2.2. A visualization of the temporal evolution of the droplet interface for the first capillary times is presented in Fig. B.10, which shows large differences in terms of shape deformations when compared to the droplet from the database, see Fig. 4.

A quantitative analysis is also shown by presenting in Fig. B.11 the temporal evolution over the first capillary time of the shape parameters for the droplets instantaneously added to the turbulent flow, and droplets from the database, Section 2.2. We confirm that the methodology presented in this work is preventing excessively fast deformations thanks to the initial no-slip condition enforced on the flow. Although this might not affect statistics for droplets with a long hold up time, it may affect statistics at a higher Weber number.

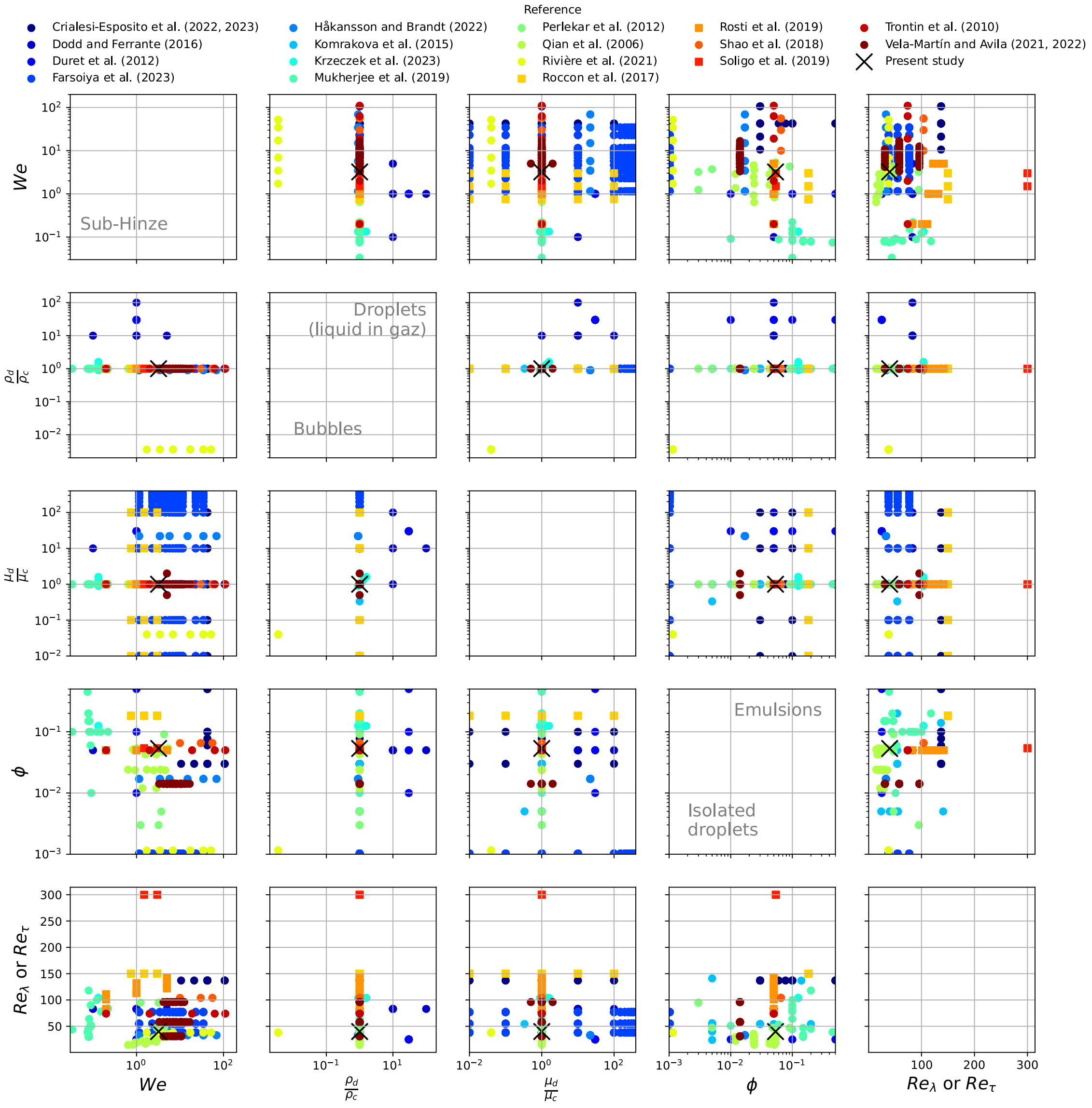

Fig. A.8. Physical parameters of interface resolved DNS of fluid–fluid turbulent flows presented in the literature. Circle markers: homogeneous isotropic turbulence; square markers, shear or wall turbulence. The parameters are explained in Table 1 and the data is given as additional material.

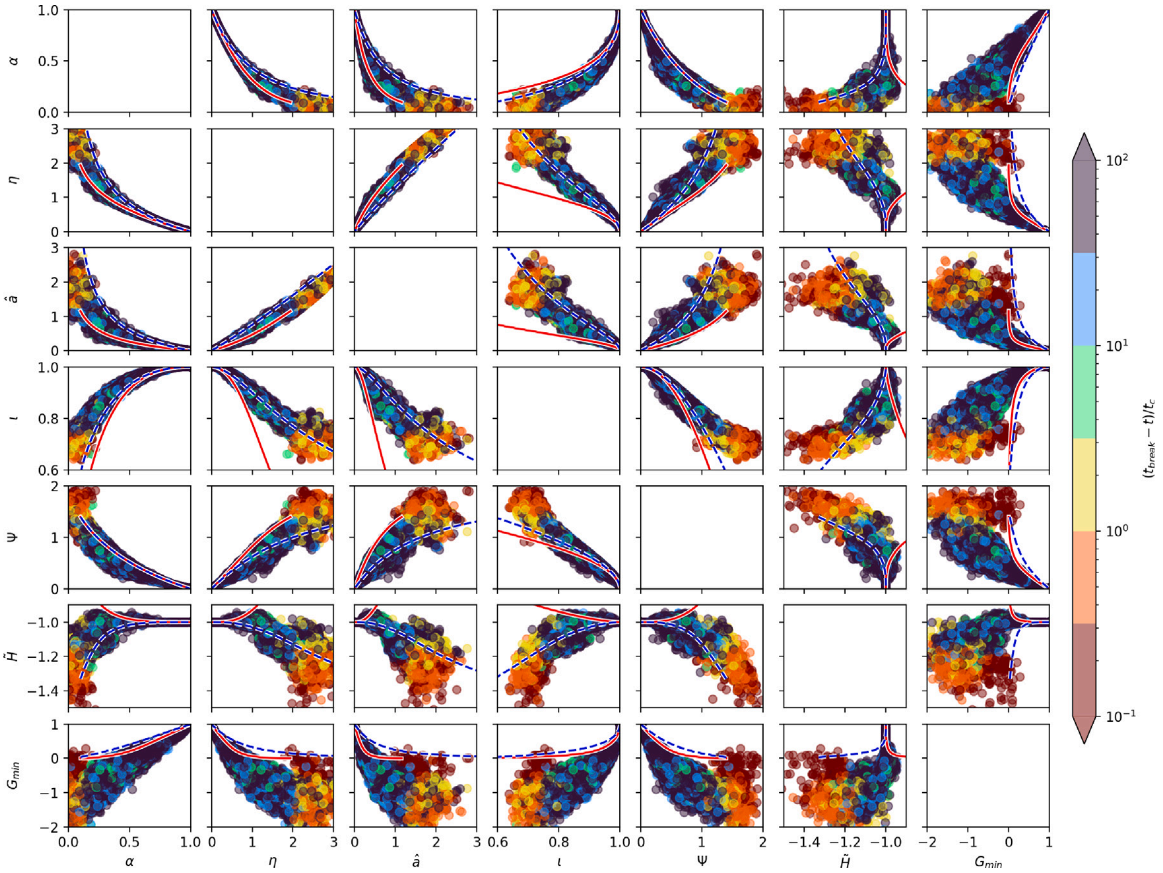

Fig. A.9. Scatter plot of shape parameters. Color by time remaining before break. The lines represent the case of oblate (solid red) and prolate (dashed blue) spheroids. The first column correspond to Fig. 6 in the manuscript.

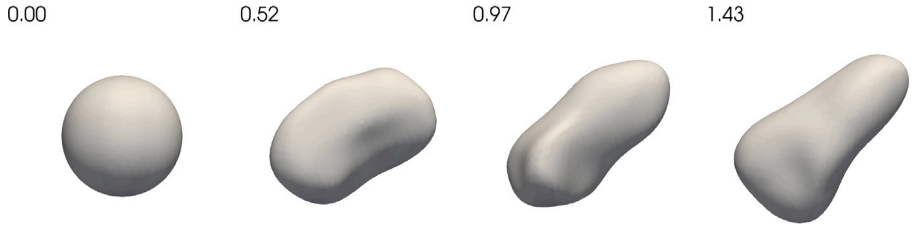

Fig. B.10. Temporal evolution of the interface of a droplet instantaneously added to the turbulent flow over the very first capillary times. Time is given dimensionless (t/t_c).

Other solution proposed in the literature is to set directly the inlet droplet velocity to zero, Rivière et al. (2022, 2021). This solution cannot be applied in the present work since the linear forcing scheme is configured to target a kinetic energy level. In our case, the droplet volume fraction and the inner flow density ratio are not negligible, thus, applying this method artificially increases the carrier flow turbulent kinetic energy to ensure that the overall domain target kinetic energy is kept.

Appendix C. Memoryless breakup

In a recent paper, Vela-Martín and Avila (2022) argued that the breakup process is memoryless for sub-Kolmogorov–Hinze droplets. In other words, the smallest droplets can survive for long turbulent times before breaking, and the breakup event is independent of the previous states of the droplets. This theory is discussed here by considering the breakup rate. For clarity, we recall that all the simulations in our database are run until a breakup event occurs.

The breakup probability function can therefore be directly computed from the definition given by Håkansson (2020) as the inverse of the average breakup time (with the hold-up time set to infinity), $\kappa = \frac{1}{\langle t_{break} \rangle}$. Here, the breakup rate obtained is $\kappa\ t_c = 8.5 \times 10^{-3}$ or $\kappa\ t_{inertia} = 0.021$.

The survival probability function for our database is shown in Fig. C.12. A very good agreement between the exponential decay, $\exp(-t\kappa)$, and the survival probability, $1 - P$, is observed up to the time $t = 160\ t_c$. Convergence for larger times requires many more realizations since only a third of the simulations from the database reach these long times.

As suggested by Coulaloglou and Tavlarides (1977), and recently confirmed by Vela-Martín and Avila (2022) for a set of parameters close to the studied ones, the breakup rate scales as $\kappa\ t_{inertia} = c_1 \exp(-c_2/We_{KH})$. In the latter, the fitting values are $c_1 = 14.8$ and $c_2 = 17.94$.[3] This correlation gives a breakup rate of $\kappa\ t_{inertia} = 0.056$, which is of the same order of magnitude as the value measured for our database.

---

[3] Since the definition of the Weber number given here differs from Vela-Martín and Avila (2022), the constant c_2 is therefore adapted.

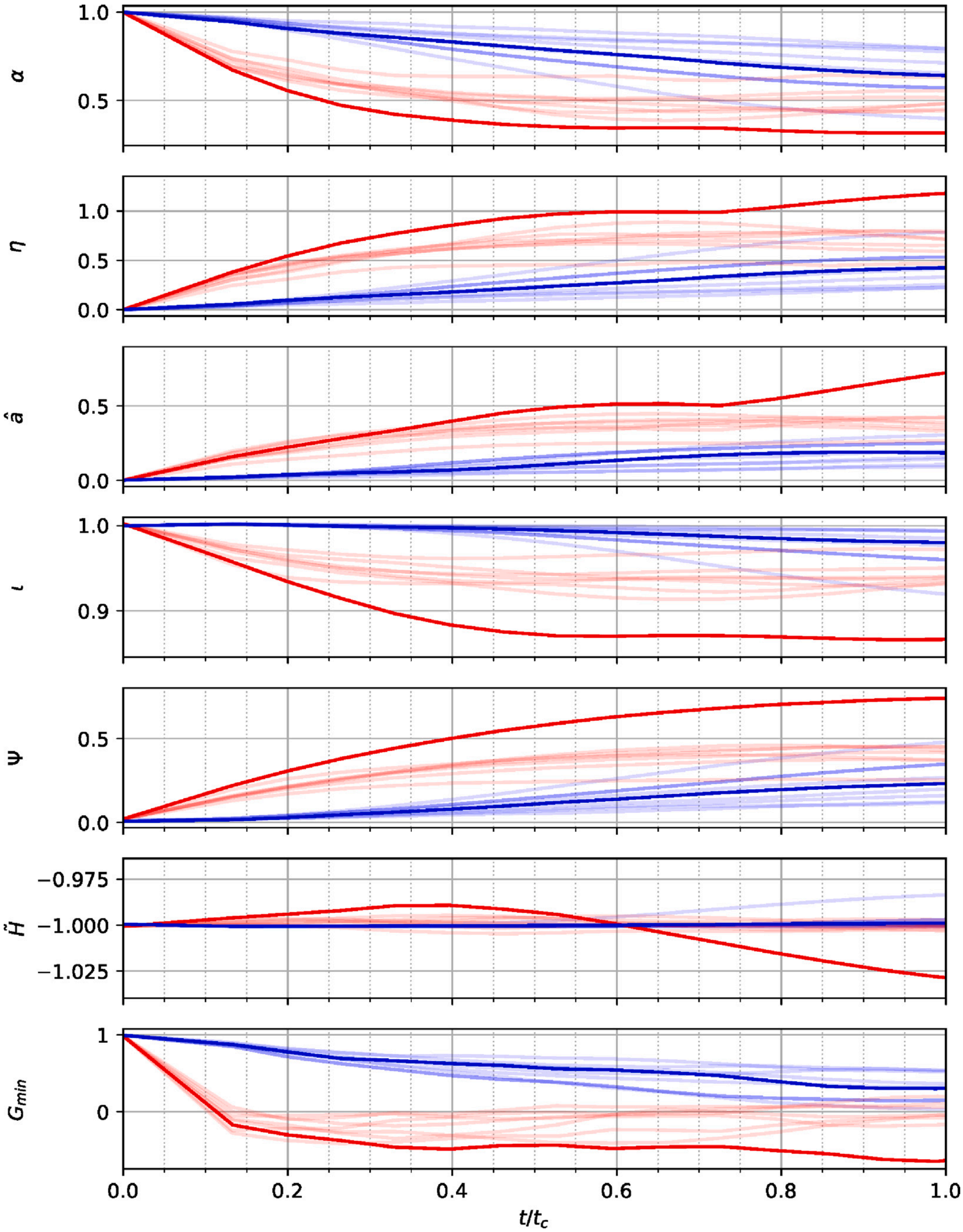

Fig. B.11. Shape parameters temporal evolution of droplets extracted from the database (blue), and droplets instantaneously added to the turbulent flow (red). The dark blue and dark red lines correspond to Figs. 4 and B.10 respectively.

A comparison with the work of Farsoiya et al. (2023) can also be made. In their work, for a given set of parameters (We, Re_λ, μ_d/μ_c) several realizations were done and the probability to break before $t = 20\ t_{inertia}$ is computed. For the closest configuration ($We = 3$ considering their definition), the number of breakup events before $t = 20\ t_{inertia}$ is 100%. If we apply the correlation given by Vela-Martín and Avila (2022) for similar conditions, the predicted breakup probability at $t = 20\ t_{inertia}$ is 67%. For our experiment, with an equivalent Weber number of 2.8, the breakup probability is 25%, similar to the breakup probability observed by Farsoiya et al. (2023) for a Weber number of 1. The discrepancies may be due to the sensitivity of the breakup rate by itself and due to the numerical initial condition as observed in Fig. C.12 for the earlier times.

When comparing the results from different authors, the Kolmogorov's approximation should be also taken into account since there is no reason that both studies have the same point-to-point correlation function $\langle(\delta u')^2\rangle(D)$ (see last paragraph on Section 2.3). Future work should be done to clarify the dependency to other parameters.

If we consider the memoryless process, all the droplets have the same probability to break regardless of their time of immersion into the turbulent flow. To give a complete picture of this problem, it is yet necessary to investigate the duration between the initial deformation state and the final breakup. During this time interval, the droplets reaches a deformation state for which the breakup does not depend on the surrounding turbulent flow and is driven by capillary (Håkansson et al., 2022). The memoryless process should not be treated as a random process related to the breakup itself, but as a random process to reach

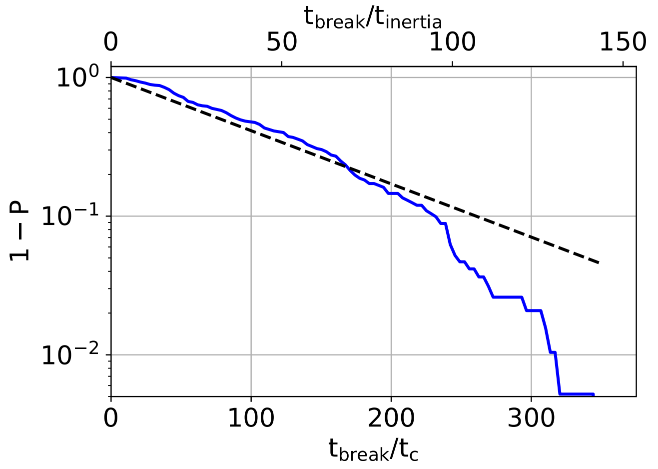

Fig. C.12. Survival probability for a given time t_{break}. Black dashed line corresponds to the constant breakup rate, $\exp(-t\kappa)$ with $\kappa = 0.021/t_{inertia}$.

this no-return state. The higher the Weber number, the greater the probability to reach this state. In other words, the theory of breakup proposed by Risso and Fabre (1998) should not be explained as droplets accumulating energy after each oscillation (as often said in the literature), but as droplets randomly reaching a no-return deformation state due to their oscillations. Characterizing this no-return state is very important, and the present work as well as the work of Håkansson et al. (2022) go in this direction.

Appendix D. Additional material

- Literature review database in csv format.
- Evolution in time of primary parameters of the realization given in Fig. 4 in csv format.
- Videos of the evolving realization given in Fig. 4. First video corresponds to Fig. 5 and second to Fig. 3.

Appendix E. Supplementary data

Supplementary material related to this article can be found online at https://doi.org/10.1016/j.ijmultiphaseflow.2024.104731.

References

Adrian, R.J., 1991. Particle-imaging techniques for experimental fluid mechanics. Annu. Rev. Fluid Mech. 23, 261–304. http://dx.doi.org/10.1146/annurev.fl.23.010191.001401.

Aniszewski, W., Brändle de Motta, J.C., 2022. A wide-range parameter study for the turbulence-interface interactions. In: 14th European Fluid Mechanics Conference.

2023. Archer web page. https://hal.science/ARCHER.

Battista, R.D., Bermejo-Moreno, I., Ménard, T., de Chaisemartin, S., Massot, M., 2019. Post-processing of two-phase DNS simulations exploiting geometrical features and topological invariants to extract flow statistics: Application to canonical objects and the collision of two droplets. In: 10th International Conference on Multiphase Flow (ICMF 2019). Rio de Janeiro, Brazil.

Blaisot, J.B., Yon, J., 2005. Droplet size and morphology characterization for dense sprays by image processing: Application to the diesel spray. Exp. Fluids 39, 977–994. http://dx.doi.org/10.1007/s00348-005-0026-4.

Breugem, W.P., 2012. A second-order accurate immersed boundary method for fully resolved simulations of particle-laden flows. J. Comput. Phys. 231, 4469–4498. http://dx.doi.org/10.1016/j.jcp.2012.02.026.

Canu, R., Duret, B., Reveillon, J., Demoulin, F.X., 2020. Curvature-based interface resolution quality (irq) indicator to assess simulation accuracy. At. Sprays 30 (1), 31–53. http://dx.doi.org/10.1615/AtomizSpr.2020033923.

Canu, R., Puggelli, S., Essadki, M., Duret, B., Menard, T., Massot, M., Reveillon, J., Demoulin, F., 2018. Where does the droplet size distribution come from? Int. J. Multiph. Flow 107, 230–245. http://dx.doi.org/10.1016/j.ijmultiphaseflow.2018.06.010.

Chen, T., Chéron, V., Zhaoli, G., Brändle de Motta, J.C., Ménard, T., Wang, L.P., 2019. Simulation of immiscible two-phase flows based on a kinetic diffuse interface approach. In: 10th International Conference on Multiphase Flow (ICMF 2019). Rio de Janeiro, Brazil, p. 10.

Chéron, V., 2020. Coupling Eulerian Interface Capturing and Lagrangian Particle Methods for Atomization Simulation (Ph.D. thesis). Rouen Normandie.

Chéron, V., Brändle de Motta, J.C., Blaisot, J.B., Menard, T., 2022. Analysis of the effect of the 2D projection on droplet shape parameters. At. Sprays 32, 59–98. http://dx.doi.org/10.1615/AtomizSpr.2022040525.

Chéron, V., Brändle de Motta, J.C., Ménard, T., Poux, A., Berlemont, A., 2023. A coupled Eulerian interface capturing and Lagrangian particle method for multiscale simulation. Comput. & Fluids 105843. http://dx.doi.org/10.1016/j.compfluid.2023.105843.

Chéron, V., Brändle de Motta, J.C., Vaudor, G., Ménard, T., Berlemont, A., 2019. From droplets to particles: Transformation criteria. In: 29th European Conference on Liquid Atomization and Spray Systems. Paris, p. 8.

Coulaloglou, C., Tavlarides, L., 1977. Description of interaction processes in agitated liquid-liquid dispersions. Chem. Eng. Sci. 32, 1289–1297. http://dx.doi.org/10.1016/0009-2509(77)85023-9.

Crialesi-Esposito, M., Chibbaro, S., Brandt, L., 2023. The interaction of droplet dynamics and turbulence cascade. Commun. Phys. 6, 5. http://dx.doi.org/10.1038/s42005-022-01122-8.

Crialesi-Esposito, M., Rosti, M.E., Chibbaro, S., Brandt, L., 2022. Modulation of homogeneous and isotropic turbulence in emulsions. J. Fluid Mech. 940 (A19), http://dx.doi.org/10.1017/jfm.2022.179.

Deike, L., 2022. Mass transfer at the ocean–atmosphere interface: The role of wave breaking, droplets, and bubbles. Annu. Rev. Fluid Mech. 54, 191–224. http://dx.doi.org/10.1146/annurev-fluid-030121-014132.

Dodd, M.S., Ferrante, A., 2016. On the interaction of Taylor length scale size droplets and isotropic turbulence. J. Fluid Mech. 806, 356–412. http://dx.doi.org/10.1017/jfm.2016.550.

Dumouchel, C., Aniszewski, W., Vu, T.T., Ménard, T., 2017. Multi-scale analysis of simulated capillary instability. Int. J. Multiph. Flow 92, 181–192. http://dx.doi.org/10.1016/j.ijmultiphaseflow.2017.03.012.

Dumouchel, C., Thiesset, F., Ménard, T., 2022. Morphology of contorted fluid structures. Int. J. Multiph. Flow 152, 104055. http://dx.doi.org/10.1016/j.ijmultiphaseflow.2022.104055.

Duret, B., Luret, G., Reveillon, J., Ménard, T., Berlemont, A., Demoulin, F.X., 2012. DNS analysis of turbulent mixing in two-phase flows. Int. J. Multiph. Flow 40, 93–105.

Eastwood, C.D., Armi, L., Lasheras, J.C., 2004. The breakup of immiscible fluids in turbulent flows. J. Fluid Mech. 502, 309–333. http://dx.doi.org/10.1017/S0022112003007730.

Farsoiya, P.K., Liu, Z., Daiss, A., Fox, R.O., Deike, L., 2023. Role of viscosity in turbulent drop break-up. J. Fluid Mech. 972. http://dx.doi.org/10.1017/jfm.2023.684.

Fedkiw, R.P., Aslam, T., Merriman, B., Osher, S., 1999. A non-oscillatory Eulerian approach to interfaces in multimaterial flows (the ghost fluid method). J. Comput. Phys. 152, 457–492. http://dx.doi.org/10.1006/jcph.1999.6236.

Ghaemi, S., Rahimi, P., Nobes, S., 2009. Assessment of parameters for distinguishing droplet shape in a spray field using image-based techniques. At. Sprays 19, 809–831. http://dx.doi.org/10.1615/AtomizSpr.v19.i9.10.

Håkansson, A., 2020. On the validity of different methods to estimate breakup frequency from single drop experiments. Chem. Eng. Sci. 227, 115908. http://dx.doi.org/10.1016/j.ces.2020.115908.

Håkansson, A., Brandt, L., 2022. Deformation and initial breakup morphology of viscous emulsion drops in isotropic homogeneous turbulence with relevance for emulsification devices. Chem. Eng. Sci. 253, 117599. http://dx.doi.org/10.1016/j.ces.2022.117599.

Håkansson, A., Crialesi-Esposito, M., Nilsson, L., Brandt, L., 2022. A criterion for when an emulsion drop undergoing turbulent deformation has reached a critically deformed state. Colloids Surf. A 129213.

Henry, H., Tegze, G., 2019. Kinetics of coarsening have dramatic effects on the microstructure: Self-similarity breakdown induced by viscosity contrast. Phys. Rev. E.

Hinze, J.O., 1955. Fundamentals of the hydrodynamic mechanism of splitting in dispersion processes. AIChE J. 1, 289–295. http://dx.doi.org/10.1002/aic.690010303.

Karimi, M., Andersson, R., 2018. An exploratory study on fluid particles breakup rate models for the entire spectrum of turbulent energy. Chem. Eng. Sci. 192, 850–863.

Karimi, M., Andersson, R., 2020. Stochastic simulation of droplet breakup in turbulence. Chem. Eng. J. 380, 122502. http://dx.doi.org/10.1016/j.cej.2019.122502.

Kolmogorov, A.N., 1949. On the breakage of drops in a turbulent flow. Dokl. Akad. Nauk 66, 825–828.

Komrakova, A.E., Eskin, D., Derksen, J.J., 2015. Numerical study of turbulent liquid-liquid dispersions. AIChE J. 61, 2618–2633. http://dx.doi.org/10.1002/aic.14821.

Krzeczek, O., Trummler, T., Trautner, E., Klein, M., 2023. Effect of the density ratio on emulsions and their segregation: A direct numerical simulation study. Energies 16 (3160), http://dx.doi.org/10.3390/en16073160.

Lalanne, B., Masbernat, O., Risso, F., 2019. A model for drop and bubble breakup frequency based on turbulence spectra. AIChE J. 65, 347–359. http://dx.doi.org/10.1002/aic.16374.

Lebas, R., Menard, T., Beau, P.A., Berlemont, A., Demoulin, F.X., 2009. Numerical simulation of primary break-up and atomization: Dns and modelling study. Int. J. Multiph. Flow 35, 247–260.

Lefebvre, A.H., McDonell, V.G., 2017. Atomization and Sprays, Second ed. CRC Press, Taylor & Francis Group, Boca Raton London New York.

Liao, Y., Lucas, D., 2009. A literature review of theoretical models for drop and bubble breakup in turbulent dispersions. Chem. Eng. Sci. 64, 3389–3406. http://dx.doi.org/10.1016/j.ces.2009.04.026.

Lister, J.R., Stone, H.A., 1998. Capillary breakup of a viscous thread surrounded by another viscous fluid. Phys. Fluids 10, 2758–2764. http://dx.doi.org/10.1063/1.869799.

Malot, H., Blaisot, J.B., 2000. Droplet size distribution and sphericity measurements of low-density sprays through image analysis. Part. Part. Syst. Charact. 17, 146–158. http://dx.doi.org/10.1002/1521-4117(200012)17:4<146::AID-PPSC146>3.0.CO;2-4.

Martinez, L.G., Duret, B., Reveillon, J., Demoulin, F., 2023. Vapor mixing in turbulent vaporizing flows. Int. J. Multiph. Flow 161, 104388. http://dx.doi.org/10.1016/j.ijmultiphaseflow.2023.104388.

Masuk, A.U.M., Salibindla, A.K.R., Ni, R., 2021. Simultaneous measurements of deforming Hinze-scale bubbles with surrounding turbulence. J. Fluid Mech. 910 (A21), http://dx.doi.org/10.1017/jfm.2020.933.

Ménard, T., Tanguy, S., Berlemont, A., 2007. Coupling level set/VOF/ghost fluid methods: Validation and application to 3D simulation of the primary break-up of a liquid jet. Int. J. Multiph. Flow 33, 510–524. http://dx.doi.org/10.1016/j.ijmultiphaseflow.2006.11.001.

2023. Mercur(v)e web page. http://docs.mercurve.rdb.is/.

Mohamed, E., Florence, D., Stéphane, D.C., Adam, L., Thibault, M., Marc, M., 2019. Statistical modeling of the gas– liquid interface using geometrical variables: Toward a unified description of the disperse and separated phase flows. Int. J. Multiph. Flow 120, 103084. http://dx.doi.org/10.1016/j.ijmultiphaseflow.2019.103084.

Mukherjee, S., Safdari, A., Shardt, O., Kenjereš, S., Van den Akker, H.E.A., 2019. Droplet– turbulence interactions and quasi-equilibrium dynamics in turbulent emulsions. J. Fluid Mech. 878, 221–276. http://dx.doi.org/10.1017/jfm.2019.654.

Ni, R., 2024. Deformation and breakup of bubbles and drops in turbulence. Annu. Rev. Fluid Mech. 51, http://dx.doi.org/10.1146/annurev-fluid-121021-034541.

O'Rourke, P.J., Amsden, A.A., 1987. The TAB method for numerical calculation of spray droplet breakup. p. 01204.

Perlekar, P., Biferale, L., Sbragaglia, M., Srivastava, S., Toschi, F., 2012. Droplet size distribution in homogeneous isotropic turbulence. Phys. Fluids 24, 065101. http://dx.doi.org/10.1063/1.4719144.

Perrard, S., Rivière, A., Mostert, W., Deike, L., 2021. Bubble deformation by a turbulent flow. J. Fluid Mech. 920 (A15), http://dx.doi.org/10.1017/jfm.2021.379.

Podczeck, F., Rahman, S., Newton, J., 1999. Evaluation of a standardised procedure to assess the shape of pellets using image analysis. Int. J. Pharm. 192, 123–138. http://dx.doi.org/10.1016/S0378-5173(99)00302-6.

Pope, S.B., 2000. Turbulent Flows. Cambridge Univ Press.

Qi, Y., Tan, S., Corbitt, N., Urbanik, C., Salibindla, A.K.R., Ni, R., 2022. Fragmentation in turbulence by small eddies. Nature Commun. 13, 469. http://dx.doi.org/10.1038/s41467-022-28092-3.

Qi, Y., Xu, X., Tan, S., Zhong, S., Wu, Q., Ni, R., 2023. Multiple timescales in bubble breakups driven by turbulence. J. Fluid Mech. (under publication).

Qian, D., McLaughlin, J.B., Sankaranarayanan, K., Sundaresan, S., Kontomaris, K., 2006. Simulation of bubble breakup dynamics in homogeneous turbulence. Chem. Eng. Commun. 193, 1038–1063. http://dx.doi.org/10.1080/00986440500354275.

Risso, F., Fabre, J., 1998. Oscillations and breakup of a bubble immersed in a turbulent field. J. Fluid Mech. 372, 323–355. http://dx.doi.org/10.1017/S0022112098002705.

Rivière, A., Mostert, W., Perrard, S., Deike, L., 2021. Sub-Hinze scale bubble production in turbulent bubble break-up. J. Fluid Mech. 917 (A40), http://dx.doi.org/10.1017/jfm.2021.243.

Rivière, A., Ruth, D.J., Mostert, W., Deike, L., Perrard, S., 2022. Capillary driven fragmentation of large gas bubbles in turbulence. Phys. Rev. Fluids 7, 083602. http://dx.doi.org/10.1103/PhysRevFluids.7.083602.

Roa, I., Renoult, M.C., Dumouchel, C., Brändle de Motta, J.C., 2023. Droplet oscillations in a turbulent flow. Front. Phys. 11, 1173521. http://dx.doi.org/10.3389/fphy.2023.1173521.

Roccon, A., De Paoli, M., Zonta, F., Soldati, A., 2017. Viscosity-modulated breakup and coalescence of large drops in bounded turbulence. Phys. Rev. Fluids 2, 083603. http://dx.doi.org/10.1103/PhysRevFluids.2.083603.

Rosales, C., Meneveau, C., 2005. Linear forcing in numerical simulations of isotropic turbulence: Physical space implementations and convergence properties. Phys. Fluids 17, 095106. http://dx.doi.org/10.1063/1.2047568.

Rosti, M.E., Ge, Z., Jain, S.S., Dodd, M.S., Brandt, L., 2019. Droplets in homogeneous shear turbulence. J. Fluid Mech. 876, 962–984. http://dx.doi.org/10.1017/jfm.2019.581.

Rudman, M., 1998. A volume-tracking method for incompressible multifluid flows with large density variations. Internat. J. Numer. Methods Fluids 28, 357–378, doi:10/fn7v9p.

Shao, C., Luo, K., Yang, Y., Fan, J., 2018. Direct numerical simulation of droplet breakup in homogeneous isotropic turbulence: The effect of the Weber number. Int. J. Multiph. Flow 107, 263–274. http://dx.doi.org/10.1016/j.ijmultiphaseflow.2018.06.009.

Soligo, G., Roccon, A., Soldati, A., 2019. Breakage, coalescence and size distribution of surfactant-laden droplets in turbulent flow. J. Fluid Mech. 881, 244–282. http://dx.doi.org/10.1017/jfm.2019.772.

Solsvik, J., Tangen, S., Jakobsen, H.A., 2013. On the constitutive equations for fluid particle breakage. Rev. Chem. Eng. 29, 241–356.

Stone, H.A., 1994. Dynamics of drop deformation and breakup in viscous fluids 26, 65–102. http://dx.doi.org/10.1146/annurev.fl.26.010194.000433.

Sussman, M., Smith, K., Hussaini, M., Ohta, M., Zhi-Wei, R., 2007. A sharp interface method for incompressible two-phase flows. J. Comput. Phys. 221, 469–505. http://dx.doi.org/10.1016/j.jcp.2006.06.020.

Trontin, P., Vincent, S., Estivalezes, J.L., Caltagirone, J.P., 2010. Direct numerical simulation of a freely decaying turbulent interfacial-flow. Int. J. Multiph. Flow 36, 891–907. http://dx.doi.org/10.1016/j.ijmultiphaseflow.2010.08.003.

Uhlmann, M., 2005. An immersed boundary method with direct forcing for the simulation of particulate flows. J. Comput. Phys. 209, 448–476. http://dx.doi.org/10.1016/j.jcp.2005.03.017.

Vaudor, G., Ménard, T., Aniszewski, W., Doring, M., Berlemont, A., 2017. A consistent mass and momentum flux computation method for two phase flows, Application to atomization process. Comput. & Fluids 152, 204–216. http://dx.doi.org/10.1016/j.compfluid.2017.04.023.

Vela-Martín, A., Avila, M., 2021. Deformation of drops by outer eddies in turbulence. J. Fluid Mech. 929 (A38), http://dx.doi.org/10.1017/jfm.2021.879.

Vela-Martín, A., Avila, M., 2022. Memoryless drop breakup in turbulence. Sci. Adv. 8, eabp9561. http://dx.doi.org/10.1126/sciadv.abp9561.

Villermaux, E., 2020. Fragmentation versus cohesion, 898, P1. http://dx.doi.org/10.1017/jfm.2020.366.

Wieringa, J., Vandieren, F., Janssen, J., Agterof, W., 1996. Droplet breakup mechanisms during emulsification in colloid mills at high dispersed phase volume fraction. Chem. Eng. Res. Des. 74, 554–562.

Zhang, J., 1996. Acceleration of five-point red-black Gauss–Seidel in multigrid for Poisson equation. Appl. Math. Comput. 80, 73–93. http://dx.doi.org/10.1016/0096-3003(95)00276-6.